Vanadyl Ethylene Glycolate for Aqueous Zinc-Ion Batteries with High Rate Capability and Ultralong Cycling Stability

Xiaoxiao Jia

A thesis

submitted in partial fulfillment of the

requirements for the degree of

Master of Science

University of Washington

2019

Committee:

Guozhong Cao

Jihui Yang

Program Authorized to Offer Degree:

Materials Science & Engineering

© Copyright 2019

Xiaoxiao Jia

University of Washington

Abstract

Vanadyl Ethylene Glycolate for Aqueous Zinc-Ion Batteries with High Rate Capability and Ultralong Cycling

Xiaoxiao Jia

Chair of the Supervisory Committee:
Guozhong Cao
Department of Materials Science & Engineering

Aqueous zinc-ion batteries (ZIBs) have shown great potential for large scale energy storage applications for its high energy density, low cost and good safety. Among the various ZIB cathode candidates, vanadium-based oxides have attracted intensive attentions due its high theoretical capacity. However, their development is still hindered by the low electronic conductivity, sluggish Zn-ion diffusion, slow electrochemical kinetics and poor structural stability. Herein, we developed a high performance vanadyl ethylene glycolate (VEG) for Zn^{2+} ions storage by modifying the vanadium oxide with organic ligands. As a result, the obtained Zn/VEG batteries exhibit a high Zn ion storage capability, a long cycling stability as well as an impressive rate performance. In addition, the intercalation pseudocapacitance behavior, the ultrafast Zn-ion diffusion kinetics as well as the high electronic conductivity of VEG are confirmed via various electrochemical analyses.

TABLE OF CONTENTS

ACKNOWLEDGEMENTS

I would first like to express my sincere gratitude to my advisor Prof. Guozhong Cao for the continuous support of my master's study and research, for his patience and immense knowledge. As my teacher and mentor, he has taught me more than I could ever give him credit for here. He has shown me, by his example, what a good scientist and person should be.

I would also like to thank Prof. Jihui Yang for serving as my thesis committee. I am gratefully indebted to his very valuable comments and suggestions.

My sincere thanks also go to Dr. Chaofeng Liu, for offering me guidance during the planning and development of this research work.

A special thanks to my parents, whose love and unfailing support are with me in whatever I pursue.

1. Introduction

The growing energy consumption and environmental concerns have been driving an ever-increasing demand for efficient and reliable electrical energy storage (ESS) systems for the utilization of renewable and clean energy resources (such as wind, solar and tide) [1-3]. The most essential criteria for developing the ideal large-scale EES systems are low cost, high reliability, good safety, environmental friendliness, energy efficiency, long cycle life, and high energy and power densities. Among numerous candidates, lithium-ion batteries with organic electrolyte, benefiting from their high energy density, long cycle life, light weight, have long been the most attractive and widely used EES systems in today's technologies, especially dominating in communication and transportation industry [4-6].

However, the application of LIBs as large-scale energy storage systems is hindered by its high cost and the safety and environmental issues. In LIBs, highly toxic and combustible organic electrolytes are used, the possible reactions between electrodes and electrolytes pose additional risks [7, 8]. Besides, the energy efficiency and power density of LIBs are unsatisfied owing to the low ionic conductivity of organic electrolytes and the formation of solid-electrolyte interphases. In addition, the cost of LIBs is relatively high due to not only the high price of materials, but also the stringent cell assembly requirements (rigorously moisture-free manufacturing conditions) [9, 10].

These challenges faced by LIBs have triggered research on sodium ion batteries (SIBs) as the primary alternative to LIBs for large-scale grid storage applications, in terms of their superior safety properties, low cost due to the natural abundance and low price of sodium resources, and similar electrochemical mechanisms to those of LIBs [11-13]. However, the

development of SIBs towards large-scale energy storage applications also encountered some inevitable issues: 1) the operation voltage is low (~0.3 V lower than Li); 2) the larger ionic size of Na^+ (1.02 Å) relative to that of Li^+ (0.76 Å), which leads to a sluggish reaction kinetics and induces a large volume variation during charging/discharging, causing unsatisfied rate performance and poor cycling life of SIBs; 3) the search for suitable electrode materials with satisfied Na storage, highly reversible capacity and long-term cyclability remains a challenge [14, 15].

As a result, the development of alternative energy storage systems that are safe, environmentally friendly, highly efficient and cost-effective is urgently needed. This has brought about particular attention to aqueous rechargeable batteries [4, 10, 16-18], which overcome the challenges of conventional LIBs by the employment of aqueous electrolytes (**Figure 1**): first, the safety issue is avoided due to the use of non-flammable aqueous electrolyte. Besides, the ionic conductivity of aqueous electrolyte (~ 1 S cm^{-1}) is significantly higher than that of organic electrolyte (~1-10 mS cm^{-1}) [19], thus offering a higher charge/discharge rate. Moreover, compared to organic LIBs, the aqueous rechargeable batteries are much cheaper and easier to be assembled [4, 10, 20].

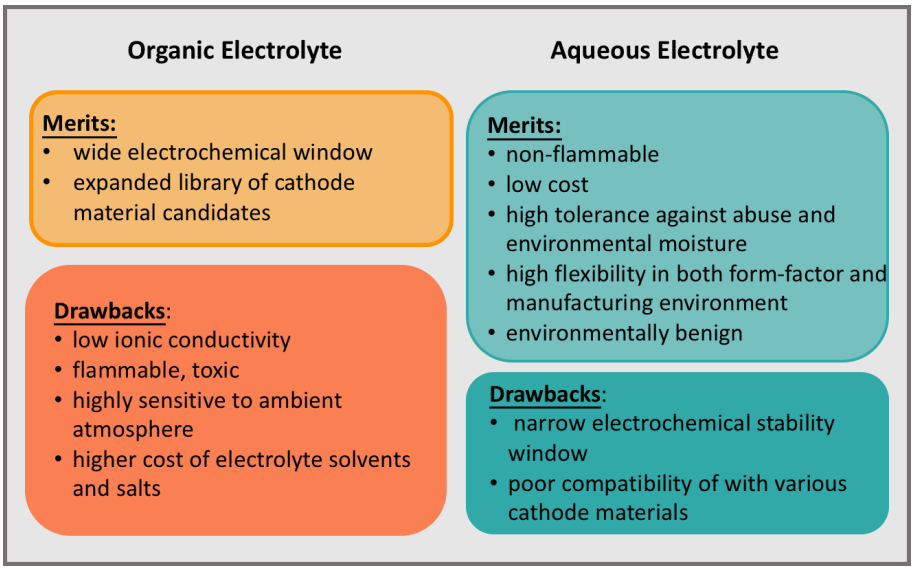

Figure 1. A comparison of the merits and drawbacks between aqueous and organic batteries

Benefiting from the intrinsic advantages of aqueous electrolytes, the aqueous rechargeable lithium ion batteries represent significant progress towards safety and environmentally benign in comparison to the conventional organic LIBs [21]. In addition, the critical issues of aqueous LIBs, low energy density and limited selection of suitable cathodes, that result from the intrinsically narrow electrochemical stability window (1.23 V) could be resolved [22, 23], enabling the successful development of high voltage, and high energy, and safety aqueous LIBs.

However, the low abundance and high cost of Li resources will hamper the practical applications of aqueous LIBs in large-scale energy storage. As an abundant and cheaper alternative to aqueous LIBs, the aqueous rechargeable Na-ion batteries have also been extensively investigated [16]. In recent years, research efforts in aqueous rechargeable battery technology also begin to shift to some other naturally abundant and low-cost

metal ions, including K-ion [24] batteries, and multivalent Zn-ion [25], Ca-ion [26], Mg-ion [27] and Al-ion [28] batteries.

Among the "beyond lithium" technologies, aqueous zinc-ion batteries (ZIBs) are particularly attractive owing to the following inherent advantages of Zn (**Table 1**): low cost arising from its natural abundance and massive production [29, 30], non-toxicity, easy and mature processing, high volumetric energy density (5851 mA h mL^{-1}) [31], high stability and compatibility in aqueous electrolyte, and the two-electron-redox properties of Zn ion leads to a high theoretical metal anode capacity (820 mAh g^{-1}) [19, 29, 32]. Therefore, the rechargeable aqueous zinc-ion batteries (ZIBs), which employ Zn metal as anode, Zn-intercalating materials as cathode, and neutral or slightly acidic Zn-containing solution as electrolyte, are promising alternative battery system for large-scale energy storage with relatively high energy and power densities as compared with other EES systems by the Ragone plot in **Figure 2**.

Table 1. Comparison of some properties of monovalent/multivalent cations as charge carrier for rechargeable batteries. [33, 34]

Metal	Ionic Radius (Å)	Standard Potential (V *vs.* SHE)	Theoretical Capacity		Abundance in the Earth's crust (ppm)	Cost ($/lb)
			Gravimetric (mAh g^{-1})	Volumetric (mAh cm^{-3})		
Li	0.76	-3.04	3862	2062	17	8-11
Na	1.02	-2.71	1166	1128	23,000	1.1-1.6
K	1.38	-2.92	686	610	15,000	3-9
Zn	0.74	-0.76	820	5851	79	0.5-1.5
Mg	0.72	-2.36	2205	3833	29,000	1-1.5
Ca	1.00	-2.86	1340	2073	50,000	-

Al	0.54	-1.67	2980	8046	82,000	0.5-1.5

Note: The price of metals is collected from METALARY (https://www.metalary.com/lithium-price/).

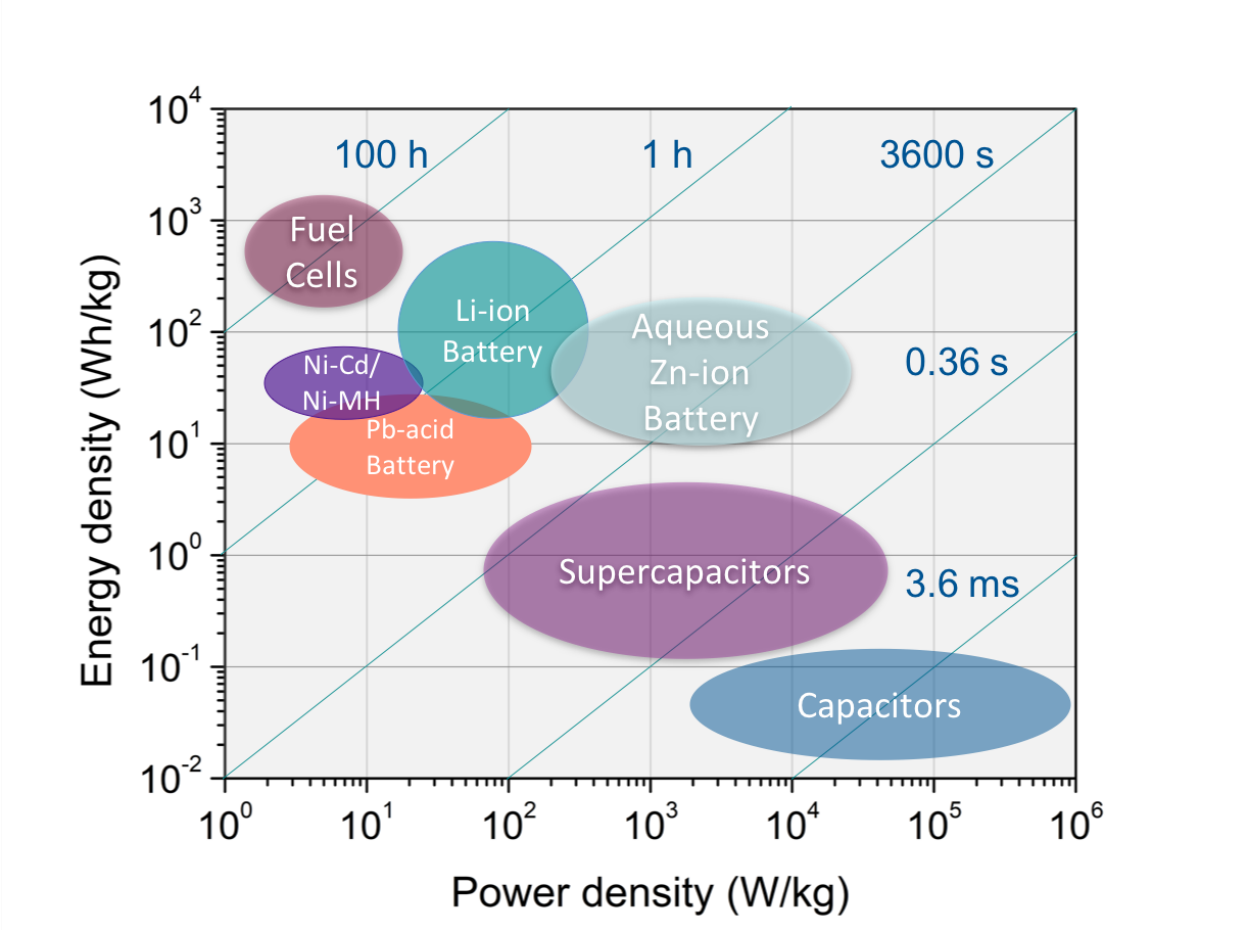

Figure 2. Ragone plot of several EES systems. Redox reaction dominated batteries present higher energy density and surface adsorption supported capacitors have higher power densities. The aqueous ZIBs probably possess the higher energy and power density together owing to the fast reaction kinetics endowed by the smaller working ion and the open frameworks of cathode materials, especially the layered vanadate hydrates. Note: the energy and power densities of aqueous Zn ion batteries are collected from the current research publications. In the commercial criteria, maybe it is a little bit lower. However, aqueous ZIBs have a huge space to improve and optimize.

Figure 3a schematically outlines the device structure and working mechanism of ZIBs. An aqueous zinc ion battery comprises of a zinc metal as anode and a layer-or tunnel-structured material as Zn^{2+} intercalation cathode, which are separated by a glass fiber or cellulose filter. The electrolyte is water-based salt solution. During the working process, Zn^{2+} will insert into or extract from cathode, and strip or plate onto the metallic anode. Pourbaix diagram of water in **Figure 3b** indicates the decomposition window change along with the pH variation. The anode and cathode must be selected such that the chemical potential of anode (μ_A) located above the lower reduction potential line, while the chemical potential of cathode reaction (μ_C) lies below the upper oxidation potential line. Or else, water will be decomposed to release the oxygen or hydrogen on the electrode surface [35]. In addition, the difference between μ_C and μ_A is termed as the open circuit voltage of a battery. Choosing a higher voltage cathode and a lower voltage anode can achieve a higher voltage battery if the electrolyte is available [36]. The cathode, anode, and electrolyte are the most essential component in an aqueous zinc ion battery. For the anode part, zinc metal anode has a higher standard potential than lithium or sodium as listed in **Table 1** and it is chemical stable in air, thus rare studies focus on the intercalation anode, except for developing the strategy to suppress the dendrite growth. Thus, in the current stage, exploiting a cathode with higher working voltage and specific capacity is very crucial to realize high energy density aqueous ZIBs for large-scale energy storage.

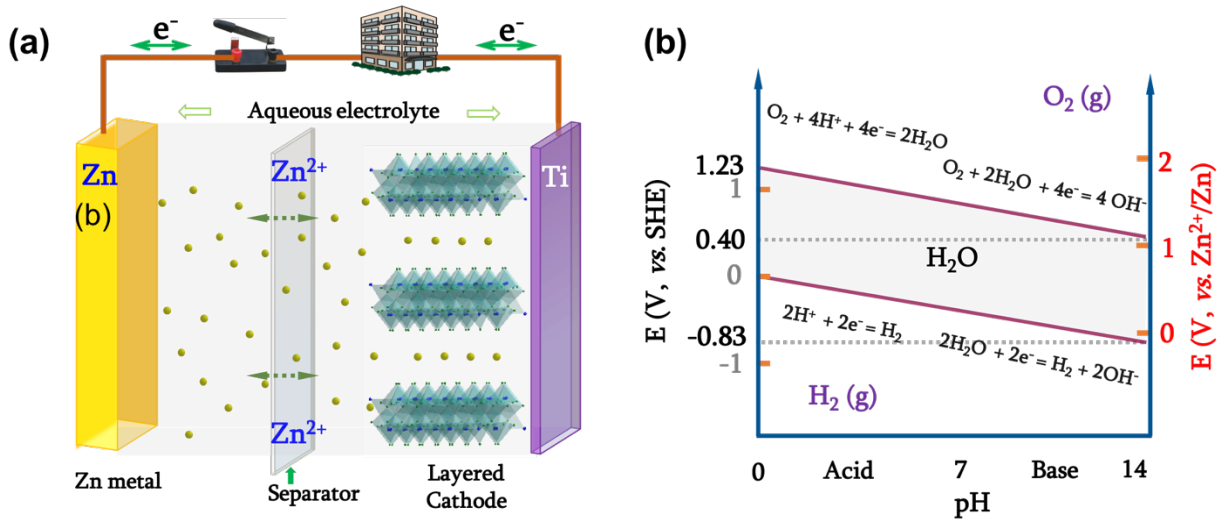

Figure 3. (a) Configuration of ZIBs. The metallic zinc anode is separated by a porous film from intercalation cathode in aqueous electrolyte. In the energy storage process, Zn^{2+} strips or plates on anode, but intercalation/deintercalation reaction happens on cathode. (b) Pourbaix diagram of water, it provides a map to design or choose an electrolyte for different cathodes for guaranteeing the battery with maximum specific capacity.

However, so far, the development of ZIBs is still in the early stage, the search for a ZIB cathode with appropriate working voltage, large reversible capacity and high structural stability still remains an obstacle. In the early stages of cathode development, a wide range of Mn-based materials have been extensively investigated as potential Zn^{2+} host materials, including α- [37], β- [32], γ- [38], δ- [39], todorokite-type [40, 41] and spinel-type MnO_2 [41]. Though the manganese based materials, such as manganese dioxide, can deliver a decent Zn^{2+} ion storage capacity of more than 200 mA h g^{-1}, [30], they usually suffer from rapid capacity fading due to the dissolution of active materials into electrolyte in the initial cycles, resulting in poor cycling stability [42, 43]. Prussian blue and its analogs, such as CuHCF [44] and ZnHCF [29], have also been reported as Zn^{2+} intercalation cathode

materials. Their large open framework structure with abundant interstitial sites is favorable for the rapid Zn^{2+} ion intercalation with no significant structural variation. However, the very low capacity (less than 70 mA h g^{-1}) and O_2 evolution problem due to the high operating voltage (~1.7 V vs. Zn) greatly restrict their further development in ZIBs [29, 45].

So, currently, the vanadium-based materials have received increasingly attention due to their large interlayer spacing and multiple oxidation states of vanadium [19, 46, 47]. However, the anhydrate V-based cathodes usually suffer from slow electrochemical kinetics and insufficient cycling stability, due to its low electronic conductivity, poor structural stability and slow ion diffusion rate [48]. For example, porous V_2O_5 in 1 M $Zn(CF_3SO_3)_2$ electrolyte delivered an initial discharge capacity of 201 mAh g^{-1}, and rapidly decreased to 73 after 90 cycles, after 240 cycles only 58% of the initial discharge capacity was retained (at 500 mA g^{-1}) [48]. Therefore, many efforts have been made to tailor the structure and composition of vanadium oxides to enhance the energy storage performance of vanadium-based materials. For example, the introduction of water molecules and the large metal ions, such as Na^+ [49], K^+ [50], Ca^{2+} [51], Zn^{2+} [52], Mg^{2+} [53] into the adjacent layers of vanadium oxides. These pre-inserted water molecules and metal ions can work as “pillars” to stabilize the structure and expand the interlayer spacing, thus contributing to an improved cycling stability and rate capability.

Herein, we report for the first time, the introduction of organic ligands into VO_x structure to enhance the ionic and electronic diffusion rate, as well as stabilize the crystal structure. This organo-vanadyl hybrid cathode material, vanadyl ethylene glycolate (VEG), is always an intermediate precursor obtained during the preparation of vanadium oxide, such as

VO_2, V_2O_5, V_2O_3 from polyol route [54, 55], however, the electrochemical property of VEG itself were rarely studied.

The VEG sample was synthesized using a facile one-step polyol method. When employed as the cathode for aqueous ZIBs, it can deliver a capacity of more than 240 mA h g^{-1} at current density of 0.5 A g^{-1}. More importantly, it exhibited excellent cyclic stability and rate capability with much improved Zn-ion transfer kinetics. The capacity retention reached 91% after almost 2000 cycles at 4.0 A g^{-1}. Furthermore, the rate performance suggested that 85% capacity maintained when the current density increased from 0.5 to 8.0 A g^{-1}. The fast Zn-ion transportation and electronic diffusion was thoroughly investigated using galvanostatic intermittent titration technique (GITT) and electrochemical impedance spectroscopy (EIS).

2. Experiments

2.1 Synthesis of VEG

All of the chemical reagents were purchased and used without further purification. In a typical synthesis, 0.025 mol ammonium metavanadate (NH_4VO_3, 99%, Sigma-Aldrich) was added into 250 mL of ethylene glycol ($C_2H_6O_2$, 99.8%, Sigma-Aldrich). The resulting mixture was heated to 110 °C with continuous stirring for 1 h in a three-neck round-bottom flask, and then heated to 160 °C for 2 h stirring, resulting in a black-colored precipitate. The precipitate was centrifuged and washed several times with ethanol to remove ethylene glycol and dried in an oven at 70 ˚C. This was further dried at 120 ˚C for 6h in a vacuum oven to obtain the final product.

2.2 Materials Characterization

The as-prepared samples were characterized by powder X-ray diffraction (XRD) on a Bruker D8 powder X-ray diffractometer (with IμS 2-D detection system) at an accelerating voltage of 50 kV and a working current of 1000 μA. The microstructures of samples were observed by scanning electron microscope (SEM, FEI Sirion) at a working voltage of 5 kV.

2.3 Electrochemical Characterization

The electrochemical performance was tested using coin cells CR2032-type assembled in air. The cathode was prepared by mixing the active materials with conductive carbon and polyvinylidene fluoride (PVDF) in weight ration of 70:20:10 using N-methyl-2-pyrrolidone (NMP) as solvent. The electrode slurry was pasted onto the titanium foil (current collector) at a mass loading of 3 - 4 mg cm^{-2}. and dried in vacuum oven at 120 °C for 12 h. Zinc foil and glass fiber membrane (Whatman, Grade GF/A) were employed as the anode and separator, respectively. The 3 M zinc trifluoromethanesulfonate ($Zn(CF_3SO_3)_2$) aqueous solution was used as electrolyte.

The Galvanostatic charge and discharge measurements were carried out on the Neware battery testing instrument at room temperature. The Cyclic voltammograms (CV) were collected on a Solartron electrochemical station at a scan rate of 0.1–1.5 mV s^{-1}. Galvanostatic intermittent titration technique (GITT) was performed on Arbin tester at a current density of 50 mA g^{-1} and the charging/discharging time and interval are 10 min for each step. The Electrochemical impedance spectroscopy (EIS) measurements was performed on the Solartron electrochemical station with an AC amplitude of 5 mV in the

frequency range from 0.01 to 10^5 Hz. All electrochemical tests were performed at room temperature and measured in the voltage window from 0.2 to 1.6 V versus Zn/Zn^{2+}.

3. Results and Discussion

3.1 Materials Characterization

The VEG powder was synthesized via a facile polyol method, as illustrated in **Figure 4**. Vanadyl ethylene glycolate has a one-dimensional chained structure that are composed of VO_5 square pyramids linked together by sharing edges (**Figure 5a**). The oxygen come from vanadyl group (V=O), chelating ligand (—OCH_2CH_2O—), and one end of two other ligands (—OCH_2CH_2O-) [56]. The open-framework and large interlayer spacing (~6.56 Å) offer facile pathways for Zn^{2+} ion diffusion. The powder X-ray diffraction pattern of the as-synthesized VEG sample was shown in **Figure 5b**. It is clear that almost all the characteristic peaks are well matched with those of standard monoclinic VEG symmetry with the *C2/c (15)* space group (PDF# 49-2497) [56]. No peaks of other impurities were detected, indicating the pure single phase VEG has been synthesized. The intensive diffraction peaks are observed at 13.5°, 14.7°, 20.5° and 27.1°, which correspond to the (110), (111), (021) and (220) crystal planes. The strong diffraction peaks indicate the high crystallinity of the VEG sample. The preferential orientation of as-synthesized VEG along the [110] direction has a large interlayer spacing of 6.56 Å, which may provide better access for Zn^{2+} ion insertion. The morphology and particle size of the as-prepared VEG powder has been studied by SEM (**Figure 5c**). The SEM images reveal that VEG composed of aggregated nanoparticles with an average size of ~ 100 nm.

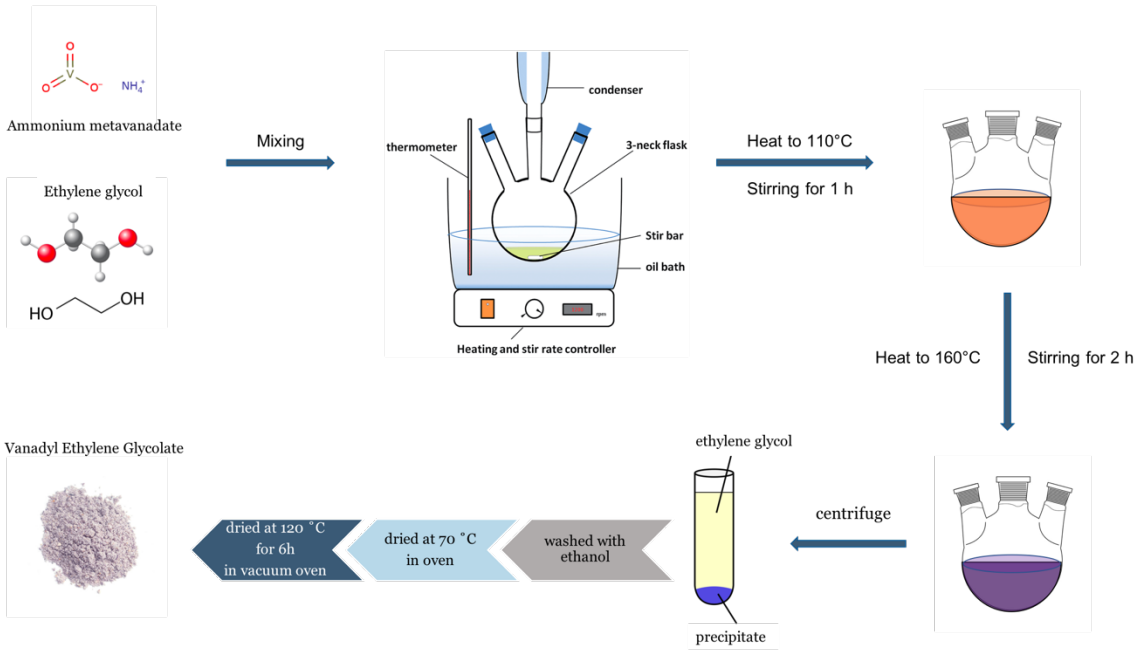

Figure 4. Schematic illustration of the synthesis route of VEG in this work.

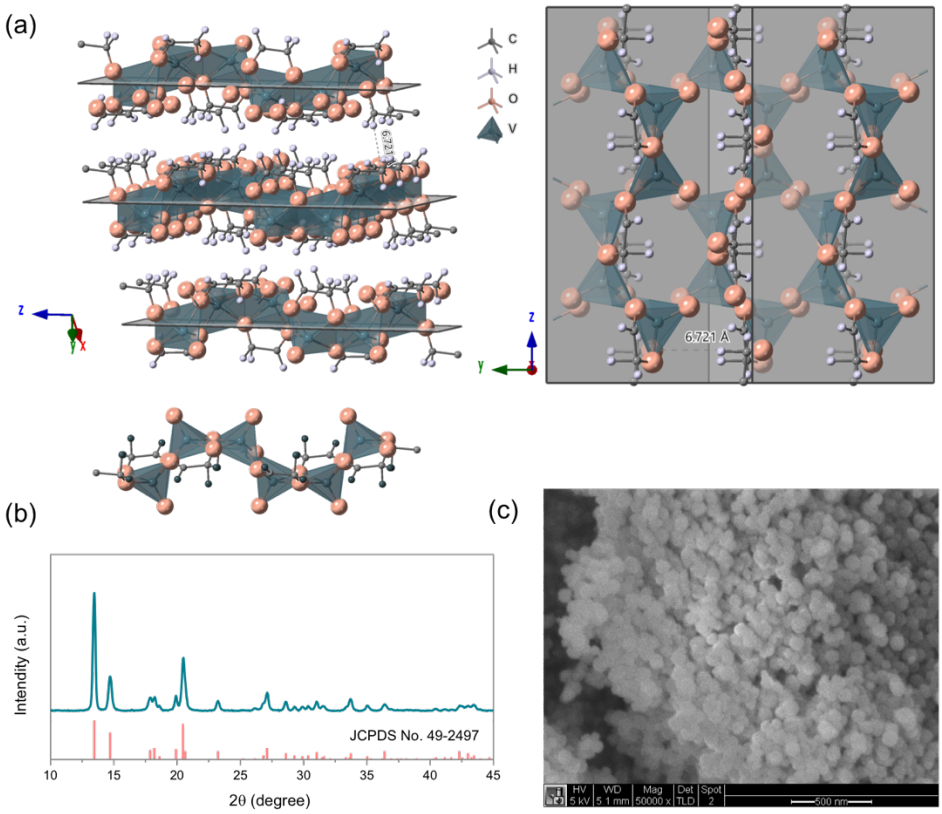

Figure 5. Material characterization of as-synthesized VEG. (a) crystal structure viewed along different directions, which showed a layered structure with chained framework. (b) XRD pattern and (c) SEM image of the as-prepared VEG.

3.2 Electrochemical Behavior

The electrochemical zinc ion storage properties were performed on the fabricated Zn/VEG cell with a 3 M $Zn(CF_3SO_3)_2$ aqueous electrolyte. **Figure 6a** displays the cyclic voltammetry (CV) curves of VEG electrode within the voltage window of 0.2–1.6 V vs Zn^{2+}/Zn at a scan rate of 0.2 mV s^{-1}. In the first cycle, the redox peaks are poorer, less well-resolved than that of the successive cycles. From the second cycles, it is clear that there are two pairs of redox peaks located at 1.04/0.91, 0.66/0.57, corresponding to the redox reaction of V^{5+}/V^{4+} and V^{4+}/V^{3+}, respectively, which are in accordance with that in V_2O_5 cathodes [57]. The cathode peaks arising from the reduction of V^{5+} to a lower valance accompanying with the electrochemical intercalation of Zn^{2+} into the host structure, while the anode peaks represent the reverse process. Notably, the CV curves in the first several cycles are significantly different from the rest of the cycles. This can be related to the gradual activation of the fresh electrode, which will be discussed in detail later. Besides, the CV profiles remain similar shapes after the fifth cycle, demonstrating the good reversibility of the VEG electrode.

The rate capability of VEG cathode was evaluated at current densities ranging from 0.5 to 4.0 A g^{-1} and then returned to 0.5 A g^{-1} (**Figure 6c**). The VEG cathode delivered a reversible specific capacity of 245, 244, 237, 225 mAh g^{-1} at the current density of 0.5, 1.0, 2.0, 4.0 A g^{-1}, respectively, with 5 cycles at each rate. Even at a high rate of 8.0 A g^{-1}, a

discharge capacity of 208 mAh g^{-1} can still be delivered. More impressively, when the applied current densities shift back from 4.0 to 0.5 A g^{-1}, a comparable or even higher capacity can be obtained at each current density. When the current density is returned to 0.5 A g^{-1}, a reversible capacity of 304 mAh g^{-1} is recovered after such a high rate cycling (40 cycles), demonstrating a superior rate capability of VEG cathode. The sudden change of discharge capacity in the initial cycle at each current density can be related to the large difference in the consecutive current rates applied abruptly on the electrode although further studies are needed to explain this. The corresponding galvanostatic charge-discharge evolution of VEG cathode at different current density are shown in **Figure 6b**. It is clear that there are two distinct voltage plateaus, which are in accordance with the two pairs of reduction/oxidation peaks in the CV curves. The features and shape of the discharge-charge curves are well maintained even at a high current density of 4.0 A g^{-1}, illustrating the excellent structural stability and reversibility of the VEG cathode.

To evaluate the long-term cycling stability of the VEG cathode, the galvanostatic discharged–charge tests were conducted at a high current density of 4.0 A g^{-1}. The maximum capacities of 205 mAh g^{-1} is reached after 100 cycles. The reversible discharge capacities of 186 mAh g^{-1} are retained after 2000 cycles and keeps its Coulombic efficiency around 100%, reaching to a preeminent capacity retention of 91%. This excellent cyclability can be attributed to both the high electrochemical reversibility and the good structural stability of the electrode materials. Notably, it is evident that the specific capacity gradually increases during the initial 100 cycles to realize a maximum, which might be attributed to the activation process upon cycling, as observed in the corresponding galvanostatic discharge profiles at current density of 4.0 A g^{-1} for different

cycles (**Figure 6e**) and the CV curves at a scan rate of 0.2 mV s^{-1} (**Figure 6a**). Similar tendency has been reported in many vanadium based materials, such as $Na_2V_6O_{16}{\cdot}3H_2O$ [58], $Zn_{0.25}V_2O_5{\cdot}nH_2O$ [52], $Na_{0.33}V_2O_5$ [49], $Ca_{0.25}$ $V_2O_5{\cdot}nH_2O$ [51], and $Mg_xV_2O_5{\cdot}nH_2O$ [53].

The general reason account for the increasing capacity for the initial few cycles is related to the gradual diffusion of the electrolyte into the inner structure, which facilitate the subsequent reaction kinetics [59]. Besides, penetration of Zn ion into the inner host structure requires definite time to attain complete equilibrium. Therefore, upon repeated cycling, the number of electrochemical sites that are penetrated by the Zn^{2+} ions will increase, thereby leading to a higher specific capacity. At a higher current density, the Zn insertion/extraction occurs at higher speed within a very short time period. Therefore, the greater the applied current density, the longer the number of cycles required for the activation process. For example, at a lower current density of 0.5 mA g-1, only 10 cycles are needed to reach a stable capacity (**Figure 6f**). However, for our materials, these explanations may not be adequate to explain the initial capacity increase. Because not only the specific capacity shows an increase, but the shape of the CV curves and the discharge-charge curves also significantly changed in the initial several cycles, suggesting the possible phase transition occurred. Hence further studies are required to identify the structure evolution as well as the composition change upon cycling.

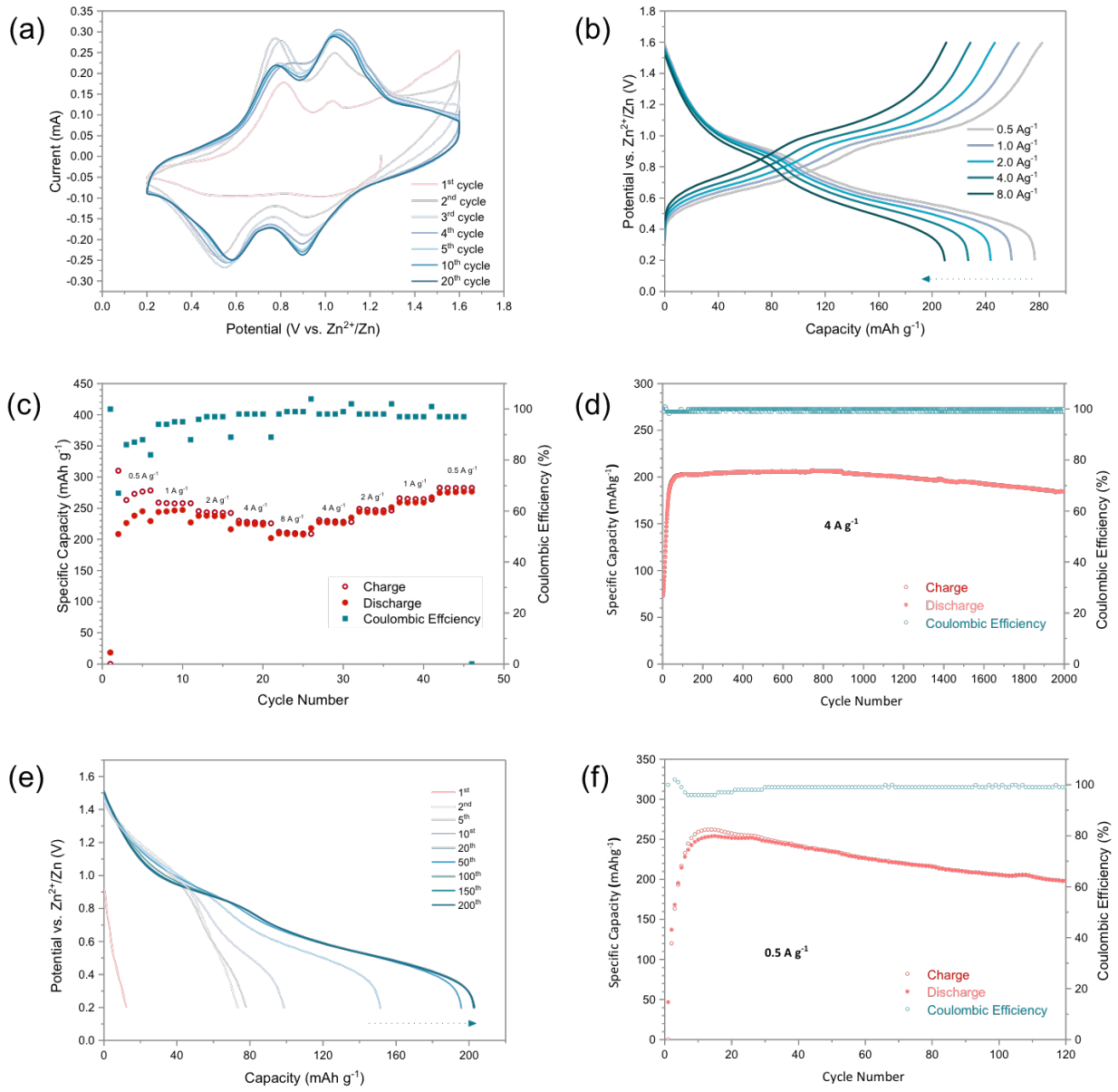

Figure 6. Electrochemical performance of Zn/VEG batteries cycling in the voltage window of 0.2-1.6 V. (a) CV curves at a scan rate of 0.2 mV s^{-1}. (b) Galvanostatic charge-discharge profiles at different current densities. (c)Rate capability at current densities from 0.5 to 8A g^{-1}. Cycling stability and the coulombic efficiency of VEG at a current density of 4 A g^{-1} (d), and its corresponding galvanostatic discharge profiles in different cycles (e). (f) Cycling stability at a current density of 0.5 A g^{-1}.

3.3 Electrochemical Kinetics Investigation

To further understand the high-rate capability and good cycling stability of VEG, the electrochemical kinetics of charge storage inside the VEG cathode was studied through analyzing the CV curves at various scan rates (**Figure 7a**). As the scan rate increase from 0.1 to 1.5 mV s^{-1} , the CV curves retain their shapes, only the anodic peaks slightly shifts to the positive direction while the cathodic peaks shifts to the opposite direction, due to the increased polarization at higher scan rates [50]. In principle, the measured peak current (i, A) of CVs obeys a power-law formula with the scan rate (v, Vs^{-1}) which can be described by: [50, 60, 61]

$$i = av^b$$

$$\log(i) = b \times \log(v) + \log(a)$$

Where a and b are adjustable parameters, with b-value can be derived from the slop of the plot of log i vs. log v, respectively. Generally, b-value varies in the range of 0.5-1.0, and there are two well defined condition: b-value = 0.5 and b-value = 1.0. b-value of 0.5 indicates a complete diffusion-controlled redox charge storage process, promoting by the faradaic intercalation/de-intercalation process of charge carriers [50, 62, 63]; while the b-value of 1.0 is representative of a strictly surface-controlled capacitive charge storage process, due to the pseudocapacitance formed via the adsorption and desorption of charge carriers at the near surface of the electrode.

For VEG, based on the log i vs. log v plot (**Figure 7b**), the b-values for four redox peaks are obtained to be 0.88, 0.91, 0.93, 0.86, respectively, implying that the Zn-ion storage in

VEG is dominated by surface-controlled capacitive process. This supports the superior rate capability of VEG.

Furthermore, the contribution of surface-controlled capacitive process and the diffusion limited redox process to the total capacity can be quantitatively separated using the equation [63]:

$$i(V) = k_1 v + k_2 v^{1/2} \quad (1)$$

where $k_1 v$ and $k_2 v^{1/2}$ represent the current contribution from the surface capacitive effects and from the diffusion-controlled insertion process, respectively [19, 31]. The above equation can also be rearranged as the following form to determine the k_1-value and k_2-value:

$$i/v^{1/2} = k_1 v^{1/2} + k_2 \quad (2)$$

As shown in **Figure 7c**, at the scan rate of 0.5 mV s^{-1}, 83% of the total current is contributed by the capacitive effects. Similarly, the capacitive- and diffusion-controlled contributions at different scan rates are calculated and summarized in **Figure 7d**. It is clearly that the capacitive contribution to the overall charge storage holds the dominant ratio and gradually increases from 71% to 90% with the increasing scan rate. The capacitive response of VEG cathode is obviously higher than that of other recently reported layered vanadium based materials, such as V_2O_5 [57] (48.5% capacitive contribution), $Ca_{0.25}V_2O_5{\cdot}xH_2O$ nanobelts (76% capacitive contribution) [51] and $Zn_3V_2O_7(OH)_2{\cdot}2H_2O$ nanowires (62% capacitive contribution) [19]. The high capacitive contribution in VEG can be attributed to the shortened ion diffusion pathways, and the

large easily accessible active surface area. This will contribute to the fast electrochemical reaction kinetics in VEG and support its high rate capability.

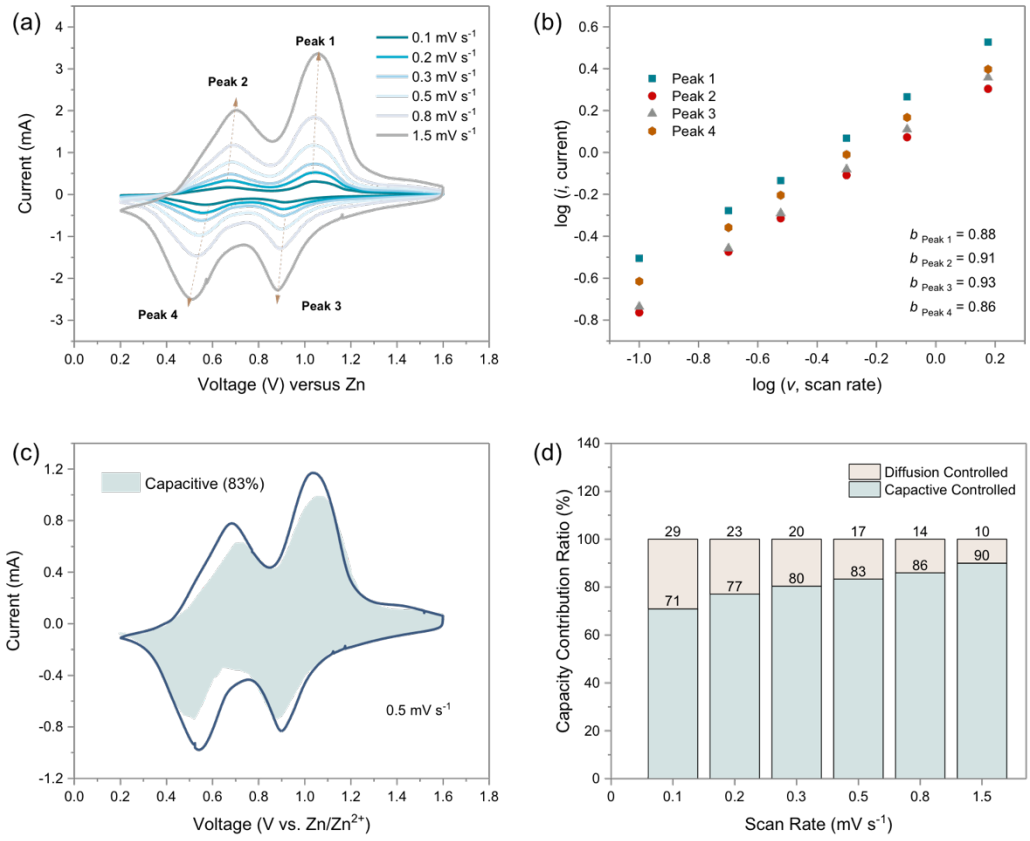

Figure 7. Electrochemical reaction kinetics of Zn/VEG batteries. (a)Cyclic voltammetry curves of VEG at different scan rates. (b) log (i) versus log (v) plots based on the CV profiles at specific peak currents. (c) CV curve at a scan rate of 0.5 mV s^{-1} of VEG with the capacitive contribution fraction shown by the shaded area. (d) Bar chart showing the capacity contribution ratio of the surface-controlled capacitive effects and the diffusion-controlled insertion process at different scan rate.

The galvanostatic intermittent titration technique (GITT) was employed to further investigate the nominal Zn^{2+}ion diffusion kinetics in the VEG cathode during cycling. In our GITT study, the cell was charged or discharged at 50 mA g^{-1} rate for 10 min, and then

relaxed for 10 min to allow the voltage to reach the equilibrium. This procedure was repeatedly applied to the cell until the charge (or discharge) voltage reached 1.6 V (or 0.2 V). The chemical diffusion coefficients of Zn^{2+} ion can be calculated based on the following equation [57, 64, 65]:

$$D_{Zn^{2+}}^{GITT} = \frac{4}{\pi}\left(\frac{m_B V_M}{M_B S}\right)^2\left(\frac{\Delta E_S}{\tau(dE_\tau/d\sqrt{\tau})}\right)^2 \left(\tau \ll \frac{L^2}{D_{Zn^{2+}}}\right) \quad (3)$$

where, τ is the current pulse duration (s), m_B is the mass of the active material (g), M_B is the molecular weight (g mol $^{-1}$), V_M is the molar volume (cm^3 mol^{-1}), S is the electrode/electrolyte contact area (cm^2), L is the thickness of the electrode, $dE_\tau/d\sqrt{\tau}$ is the slope of the linearized region of the potential E_τ (V) during the current pulse in the duration time τ (s). ΔE_S is the difference in the open circuit voltage measured at the end of the relaxation period for two successive steps (as illustrated in Figure 8c). If sufficiently small currents are applied for short time intervals, so that the variation of cell voltage (ΔE_τ) during titration was shown to be a linear relationship vs. $\tau^{1/2}$ (as shown in Figure 8d), the above equation can be further simplified as [66]

$$D_{Zn^{2+}}^{GITT} = \frac{4}{\pi\tau}\left(\frac{m_B V_M}{M_B S}\right)^2\left(\frac{\Delta E_S}{\Delta E_\tau}\right)^2 \quad . \quad (4)$$

The discharge/charge curves in GITT measurements in the 2nd cycles and the corresponding diffusion coefficients of Zn^{2+} are shown in **Figure 8 a, b**. The D_{Zn2+} values were estimated to be in the order of 10^{-9} - 10^{-11} cm^2s^{-1}, which is much higher than that of the bulk V_2O_5 cathode [57] and even comparable to the Li diffusion coefficient in V_2O_5 cathode [67]. This clearly demonstrates high ionic transportation rate in the as-prepared VEG cathode, which can be ascribed to its shortened diffusion path and large interlayer spacing.

In addition, upon discharging, there is a tendency that the $D_{Zn^{2+}}$ gradually decreased, which may be ascribed to the increased coulombic interaction between the inserted Zn^{2+} ions in the host structure. With further discharging, the interlayer spacing will be expanded due to the large sized V^{4+} formed from the reduction of V^{5+}, which might be responsible for the later recovery of the Zn^{2+} ion diffusion rate. Correspondingly, $D_{Zn^{2+}}$ value first decreases and then increases upon charging. The decrease of $D_{Zn^{2+}}$ is probably due to the lattice shrinkage upon the oxidation of V^{4+} to V^{5+}, while the latter increase might be attributed to the weaker coulombic interaction between the Zn^{2+} ions in the host structure.

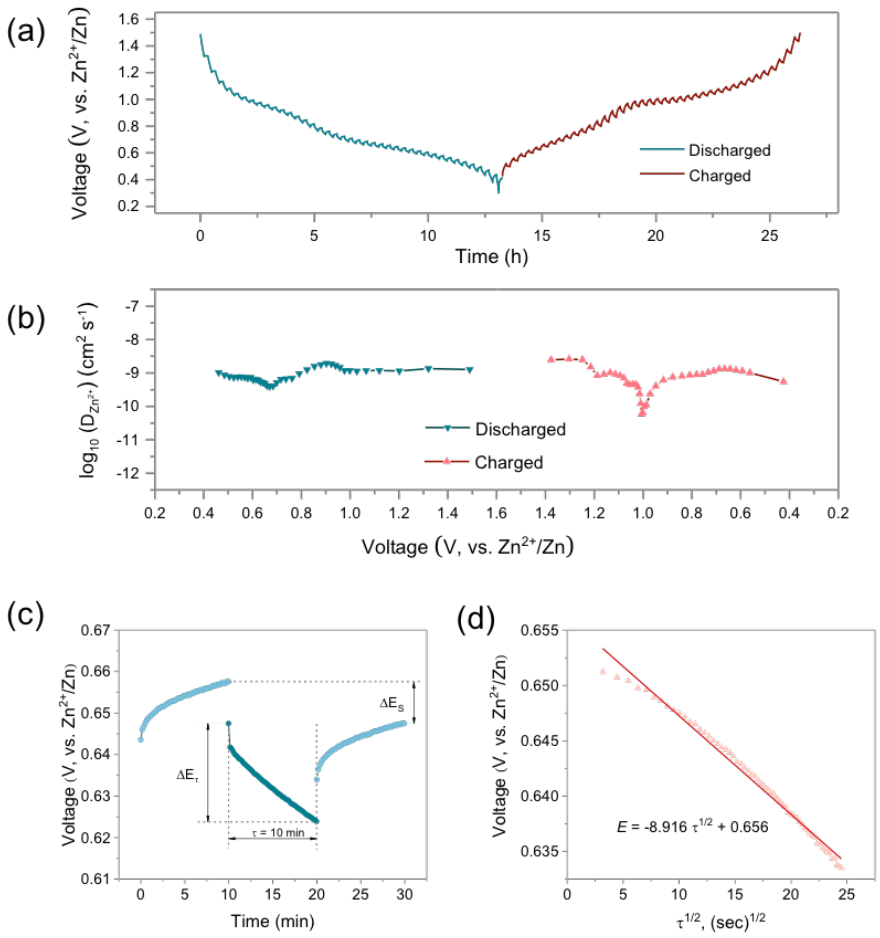

Figure 8. (a) The galvanostatic intermittent titration technique (GITT) profiles at 0.05 A g^{-1} and (b) the calculated Zn^{2+} diffusion coefficient in VEG. (c) Demonstration of a selected single step of the GITT profile during charging. The voltage profile before, during and after a constant current pulse with schematic labeling of different parameters. (d) Plot of voltage against τ1/2 to show the linear fit.

Besides the beneficial ionic diffusion, the VEG cathode also favors charge transfer, as viewed from the electrochemical impedance spectroscopy (EIS) analysis (**Figure 9**). **Figure 9** exhibits the Nyquist plots of VEG, which consists of a semicircle in the high-frequency region, attributing to the charge-transfer process between the electrolyte and the electrode, and a straight line with a slope of approximately 45° in medium-frequency region (1-0.1 Hz), which corresponds to Warburg impedance that are associated with Zn^{2+} ions diffusion in the bulk VEG electrode, and a steeper straight line in a low frequency region, atributing to the onset of finite length diffusion [68, 69].

The charge transfer resistance (R_{ct}) can be obtained by the intercept of the high-frequency semicircle on the real axis. The Zn-ion diffusion coefficient in the VEG electrodes can be calculated according to the following equations [69, 70]:

$$D_{Zn^{2+}}^{EIS} = \frac{R^2T^2}{2A^2n^4F^4C^2\sigma_W{}^2} \quad (5)$$

where A is the surface area of cathode (A = 0.875 cm^2), *n* is number of reactive electrons per chemical formula (n = 2), F the Faraday constant (96,485 C mol^{-1}), C the molar concentration of Zn^{2+} (C = 3.0 × 10^{-3} mol cm^{-3}), R the gas constant (8.314 J $mol^{-1}K^{-1}$), T the absolute temperature (298 K), σ_w the Warburg coefficient, which can be obtained from the slope of Z′ vs. $\omega^{-1/2}$ plots (ω: angular frequency) in medium-frequency region (1-0.1 Hz).

Figure 9b shows the relationship between Z′ and $\omega^{-1/2}$ in medium-frequency region (1-0.1 Hz). The charge transfer resistance (R_{ct}) and the Zn ion diffusion coefficient ($D_{Zn^{2+}}$) in VEG after CV cycles are calculated and plotted in **Figure 9c**. It is noted that after the first cycle, the R_{ct} reduced sharply in the initial three cycles (85 Ω after the 1st cycle and 8 Ω after the 3rd cycle) and then maintained a low value upon further cycling (16 Ω after 10 cycles). Correspondingly, the $D_{Zn^{2+}}$ values increased dramatically from 10^{-12} to the 10^{-11} cm^2s^{-1} and remained stable afterwards. This is consistent with the initial activation process observed from CV curves and the galvanostatic discharged–charge curves. The charge transfer resistance of VEG is much lower than many reported vanadium oxides, such as $Na_{0.33}V_2O_5$ nanosheet-graphene hybrids (158 Ω) [71]. This low ion diffusion barrier and the enhanced electronic conductivity of VEG might be attributed to its shortened transport pathways, the good interparticle contacts, and the increased available and easily accessible active surface area enabled by the nano-cubed morphology.

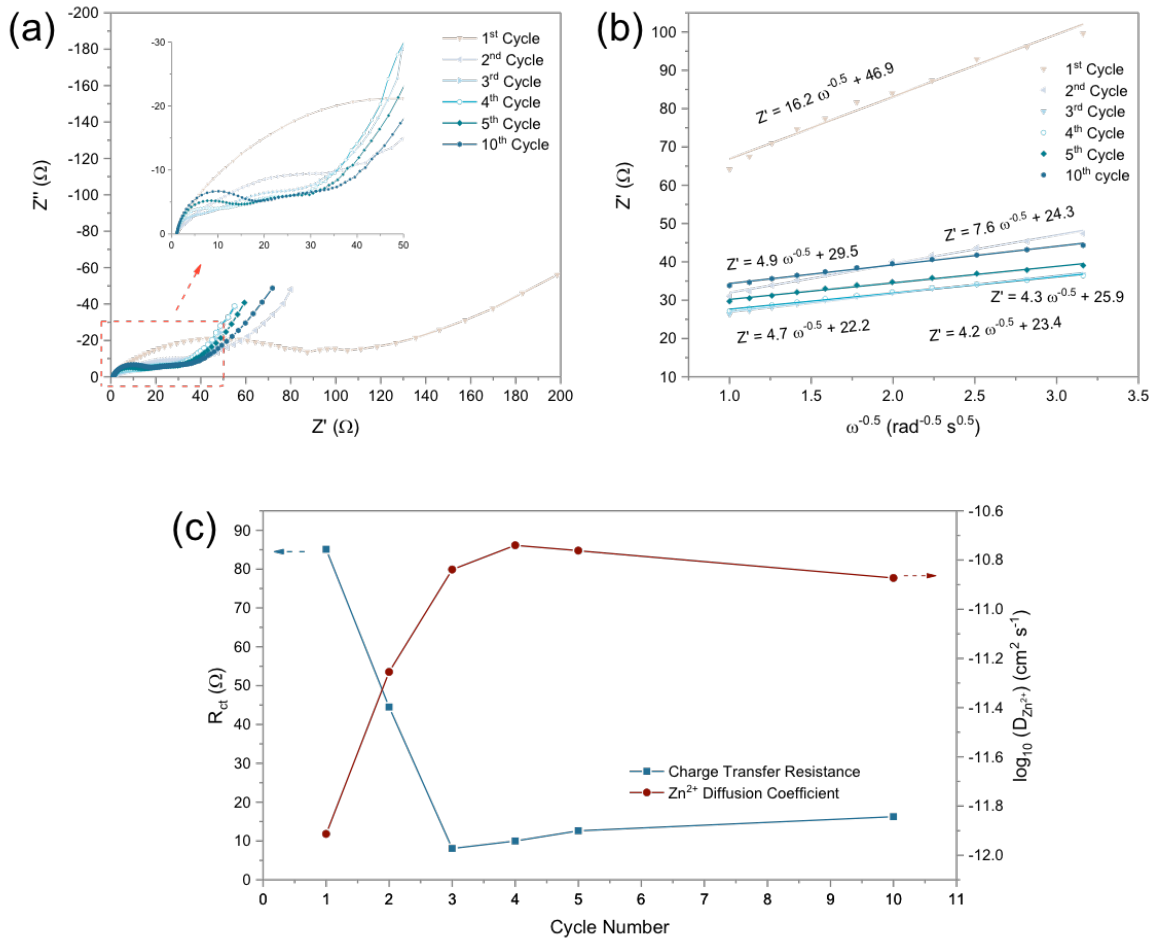

Figure 9. (a) The Nyquist plot of VEG cathode (b) the relationship between the real part of impedance Z' and $\omega^{-1/2}$ (ω is the angular frequency) at low-frequency region. (c) the variation of charge transfer resistance and the diffusion coefficient of Zn ions in VEG during the first 10 cycles.

Table 2. The charge transfer resistances (R_{ct}) and the nominal Zn ion diffusion coefficients ($D_{Zn^{2+}}$) from EIS tests.

Test Stage	R_{ct} (Ω)	D_{Zn2+} (cm^2/s)
1st cycle	85	1.2×10^{-12}
2nd cycle	44	5.6×10^{-12}
3rd cycle	8	1.4×10^{-11}
4th cycle	9	1.8×10^{-11}
5th cycle	12	1.7×10^{-11}
10th cycle	16	1.3×10^{-11}

4. Conclusions

In conclusion, we develop a novel organic–inorganic vanadyl ethylene glycolate cathode materials as a new feasible cathode for aqueous ZIBs. By introducing organic ligands, the crystal structure of VO_x can be stabilized upon cycling. Benefiting from the abundant tunnel diffusion pathways, the VEG cathode demonstrates a predominantly capacitive behavior, the low charge transfer barrier (R_{ct} ~31 Ω) and Zn ions (nominal $D_{Zn^{2+}}$ reaching 10^{-9} cm^2 s^{-1}). Thus, this aqueous Zn/VEG battery delivers a long-term cycling stability with 91% capacity retention after 2000 cycles at 4.0 A g^{-1} and an impressive rate capability with 85% capacity maintained when the current density increased from 0.5 to 8.0 A g^{-1}, showing promising application as ZIB cathode. This study provide insight into the molecular manipulation of vanadium oxide structure and access to improve bulk-

phase Zn-diffusion kinetics, which would shed light on the rapid development of ZIB cathode with high rate capability.

5. Future Work

Future work concerns deeper analysis of Zn^{2+} storage mechanism in VEG cathode, comparison of electrochemical performance of VEG with that of other vanadium oxides, or the design of other optimized organic-inorganic hybrids as ZIB cathode.

First, in order to gain insight into the Zn^{2+} storage mechanism in VEG cathode, the structural evolution and the changes in valence state of vanadium accompanying Zn^{2+} intercalation/de-intercalation in VEG, as well as the phase transformation and morphological evolution during cycling should be characterized by the *ex situ* XRD analysis and *ex situ* X-ray photoelectron spectroscopy analysis at different discharged/charged states, combined by the element mappings of Zn, V and O by energy-dispersive X-ray spectroscopy.

Second, further calcine the obtained VEG powder at different temperature to synthesis the VO_2 and V_2O_5, and compared their electrochemical performance as ZIB cathode with that of VEG.

Third, different kinds of inorganic host structure and the guest organic ligands can be carefully selected to design the other optimized organic-inorganic hybrids as ZIB cathode.

BIBLIOGRAPHY

1. Larcher, D. and J.M. Tarascon, *Towards greener and more sustainable batteries for electrical energy storage*. Nature Chemistry, 2014. 7: p. 19.
2. Hosenuzzaman, M., et al., *Global prospects, progress, policies, and environmental impact of solar photovoltaic power generation*. Renewable and Sustainable Energy Reviews, 2015. 41: p. 284-297.
3. Li, Q., et al., *Solar energy storage in the rechargeable batteries*. Nano Today, 2017. 16: p. 46-60.
4. Tang, W., et al., *Aqueous rechargeable lithium batteries as an energy storage system of superfast charging*. Energy & Environmental Science, 2013. 6(7): p. 2093-2104.
5. Manthiram, A., *An Outlook on Lithium Ion Battery Technology*. ACS Central Science, 2017. 3(10): p. 1063-1069.
6. Kim, T.-H., et al., *The Current Move of Lithium Ion Batteries Towards the Next Phase*. Advanced Energy Materials, 2012. 2(7): p. 860-872.
7. Liu, B., et al., *Safety issues caused by internal short circuits in lithium-ion batteries*. Journal of Materials Chemistry A, 2018. 6(43): p. 21475-21484.
8. Abada, S., et al., *Safety focused modeling of lithium-ion batteries: A review*. Journal of Power Sources, 2016. 306: p. 178-192.
9. Liu, J., et al., *Aqueous Rechargeable Batteries for Large-scale Energy Storage*. Israel Journal of Chemistry, 2015. 55(5): p. 521-536.
10. Kim, H., et al., *Aqueous Rechargeable Li and Na Ion Batteries*. Chemical Reviews, 2014. 114(23): p. 11788-11827.
11. Kubota, K. and S. Komaba, *Review—Practical Issues and Future Perspective for Na-Ion Batteries*. Journal of The Electrochemical Society, 2015. 162(14): p. A2538-A2550.
12. Deng, J., et al., *Sodium-Ion Batteries: From Academic Research to Practical Commercialization*. Advanced Energy Materials, 2017. 8(4): p. 1701428.
13. Yabuuchi, N., et al., *Research Development on Sodium-Ion Batteries*. Chemical Reviews, 2014. 114(23): p. 11636-11682.
14. Hwang, J.-Y., S.-T. Myung, and Y.-K. Sun, *Sodium-ion batteries: present and future*. Chemical Society Reviews, 2017. 46(12): p. 3529-3614.
15. Li, L., et al., *Recent progress on sodium ion batteries: potential high-performance anodes*. Energy & Environmental Science, 2018. 11(9): p. 2310-2340.
16. Bin, D., et al., *Progress in Aqueous Rechargeable Sodium-Ion Batteries*. Advanced Energy Materials, 2018. 8(17): p. 1703008.
17. Alias, N. and A.A. Mohamad, *Advances of aqueous rechargeable lithium-ion battery: A review*. Journal of Power Sources, 2015. 274: p. 237-251.
18. Xing, Z., et al., *Aqueous intercalation-type electrode materials for grid-level energy storage: Beyond the limits of lithium and sodium*. Nano Energy, 2018. 50: p. 229-244.
19. Xia, C., et al., *Rechargeable Aqueous Zinc-Ion Battery Based on Porous Framework Zinc Pyrovanadate Intercalation Cathode*. Advanced Materials, 2018. 30(5).

20. Liu, J., et al., *Progress in aqueous rechargeable batteries*. Green Energy & Environment, 2018. 3(1): p. 20-41.
21. Wang, Y., J. Yi, and Y. Xia, *Recent Progress in Aqueous Lithium-Ion Batteries*. Advanced Energy Materials, 2012. 2(7): p. 830-840.
22. Suo, L., et al., *"Water-in-salt" electrolyte enables high-voltage aqueous lithium-ion chemistries*. Science, 2015. 350(6263): p. 938.
23. Yamada, Y., et al., *Hydrate-melt electrolytes for high-energy-density aqueous batteries*. Nature Energy, 2016. 1: p. 16129.
24. Kim, H., et al., *Recent Progress and Perspective in Electrode Materials for K-Ion Batteries*. Advanced Energy Materials, 2017. 8(9): p. 1702384.
25. Song, M., et al., *Recent Advances in Zn-Ion Batteries*. Advanced Functional Materials, 2018. 28(41): p. 1802564.
26. Huang, J., et al., *Recent Progress of Rechargeable Batteries Using Mild Aqueous Electrolytes*. Small Methods, 2018. 0(0): p. 1800272.
27. Park, M.-S., et al., *Recent Advances in Rechargeable Magnesium Battery Technology: A Review of the Field's Current Status and Prospects*. Israel Journal of Chemistry, 2015. 55(5): p. 570-585.
28. Das, S.K., S. Mahapatra, and H. Lahan, *Aluminium-ion batteries: developments and challenges*. Journal of Materials Chemistry A, 2017. 5(14): p. 6347-6367.
29. Zhang, L., et al., *Towards High-Voltage Aqueous Metal-Ion Batteries Beyond 1.5 V: The Zinc/Zinc Hexacyanoferrate System*. Advanced Energy Materials, 2014. 5(2): p. 1400930.
30. Xu, C., et al., *Energetic zinc ion chemistry: the rechargeable zinc ion battery*. Angewandte Chemie International Edition, 2012. 51(4): p. 933-935.
31. He, P., et al., *High-Performance Aqueous Zinc-Ion Battery Based on Layered H2V3O8 Nanowire Cathode*. Small, 2017. 13(47).
32. Zhang, N., et al., *Rechargeable aqueous zinc-manganese dioxide batteries with high energy and power densities*. Nature Communications, 2017. 8(1): p. 405.
33. Andrews, J.L. and S. Banerjee, *It's Not Over until the Big Ion Dances: Potassium Gets Its Groove On*. Joule, 2018. 2(11): p. 2194-2197.
34. Massé, R., E. Uchaker, and G. Cao, *Beyond Li-ion: electrode materials for sodium- and magnesium-ion batteries*. Science China Materials, 2015. 58(9): p. 715-766.
35. Konarov, A., et al., *Present and Future Perspective on Electrode Materials for Rechargeable Zinc-Ion Batteries*. ACS Energy Letters, 2018. 3(10): p. 2620-2640.
36. Liu, C., et al., *A promising cathode for Li-ion batteries: Li3V2(PO4)3*. Energy Storage Materials, 2016. 4: p. 15-58.
37. Lee, B., et al., *Elucidating the intercalation mechanism of zinc ions into α-MnO2 for rechargeable zinc batteries*. Chemical Communications, 2015. 51(45): p. 9265-9268.
38. Alfaruqi, M.H., et al., *Electrochemically Induced Structural Transformation in a γ-MnO2 Cathode of a High Capacity Zinc-Ion Battery System*. Chemistry of Materials, 2015. 27(10): p. 3609-3620.
39. Kim, S.H. and S.M. Oh, *Degradation mechanism of layered MnO2 cathodes in Zn/ZnSO4/MnO2 rechargeable cells*. Journal of Power Sources, 1998. 72(2): p. 150-158.

40. Lee, J., et al., *Todorokite-type MnO2 as a zinc-ion intercalating material.* Electrochimica Acta, 2013. 112: p. 138-143.
41. Hao, J.W., et al., *Electrochemically induced spinel-layered phase transition of Mn3O4 in high performance neutral aqueous rechargeable zinc battery.* Electrochimica Acta, 2018. 259: p. 170-178.
42. Xu, D., et al., *Preparation and Characterization of MnO2/acid-treated CNT Nanocomposites for Energy Storage with Zinc Ions.* Electrochimica Acta, 2014. 133: p. 254-261.
43. Alfaruqi, M.H., et al., *Enhanced reversible divalent zinc storage in a structurally stable α-MnO2 nanorod electrode.* Journal of Power Sources, 2015. 288: p. 320-327.
44. Jia, Z.J., B.G. Wang, and Y. Wang, *Copper hexacyanoferrate with a well-defined open framework as a positive electrode for aqueous zinc ion batteries.* Materials Chemistry and Physics, 2015. 149: p. 601-606.
45. Trócoli, R. and F. La Mantia, *An Aqueous Zinc-Ion Battery Based on Copper Hexacyanoferrate.* ChemSusChem, 2014. 8(3): p. 481-485.
46. Alfaruqi, M.H., et al., *Electrochemical Zinc Intercalation in Lithium Vanadium Oxide: A High-Capacity Zinc-Ion Battery Cathode.* Chemistry of Materials, 2017. 29(4): p. 1684-1694.
47. He, P., et al., *Layered VS2 Nanosheet-Based Aqueous Zn Ion Battery Cathode.* Advanced Energy Materials, 2017. 7(11): p. 1601920.
48. Hu, P., et al., *Zn/V2O5 Aqueous Hybrid-Ion Battery with High Voltage Platform and Long Cycle Life.* Acs Applied Materials & Interfaces, 2017. 9(49): p. 42717-42722.
49. He, P., et al., *Sodium Ion Stabilized Vanadium Oxide Nanowire Cathode for High-Performance Zinc-Ion Batteries.* Advanced Energy Materials, 2018. 8(10).
50. Tang, B., et al., *Potassium vanadates with stable structure and fast ion diffusion channel as cathode for rechargeable aqueous zinc-ion batteries.* Nano Energy, 2018. 51: p. 579-587.
51. Xia, C., et al., *Highly Stable Aqueous Zinc-Ion Storage Using a Layered Calcium Vanadium Oxide Bronze Cathode.* Angewandte Chemie-International Edition, 2018. 57(15): p. 3943-3948.
52. Kundu, D., et al., *A high-capacity and long-life aqueous rechargeable zinc battery using a metal oxide intercalation cathode.* Nature Energy, 2016. 1(10): p. 16119.
53. Ming, F., et al., *Layered MgxV2O5·nH2O as Cathode Material for High-Performance Aqueous Zinc Ion Batteries.* ACS Energy Letters, 2018. 3(10): p. 2602-2609.
54. Mjejri, I., A. Rougier, and M. Gaudon, *Low-Cost and Facile Synthesis of the Vanadium Oxides V2O3, VO2, and V2O5 and Their Magnetic, Thermochromic and Electrochromic Properties.* Inorganic Chemistry, 2017. 56(3): p. 1734-1741.
55. Ragupathy, P., et al., *Preparation of Nanostrip V2O5 by the Polyol Method and Its Electrochemical Characterization as Cathode Material for Rechargeable Lithium Batteries.* The Journal of Physical Chemistry C, 2008. 112(42): p. 16700-16707.
56. Weeks, C., et al., *The one dimensional chain structures of vanadyl glycolate and vanadyl acetate.* Journal of Materials Chemistry, 2003. 13(6): p. 1420-1423.

57. Zhang, N., et al., *Rechargeable Aqueous Zn–V2O5 Battery with High Energy Density and Long Cycle Life*. ACS Energy Letters, 2018. 3(6): p. 1366-1372.
58. Soundharrajan, V., et al., *Na2V6O16·3H2O Barnesite Nanorod: An Open Door to Display a Stable and High Energy for Aqueous Rechargeable Zn-Ion Batteries as Cathodes*. Nano Letters, 2018. 18(4): p. 2402-2410.
59. Sambandam, B., et al., *K2V6O16·2.7H2O nanorod cathode: an advanced intercalation system for high energy aqueous rechargeable Zn-ion batteries*. Journal of Materials Chemistry A, 2018. 6(32): p. 15530-15539.
60. Ding, J., et al., *Ultrafast Zn2+ Intercalation and Deintercalation in Vanadium Dioxide*. Advanced Materials, 2018. 30(26): p. 1800762.
61. Dong, X., et al., *Environmentally-friendly aqueous Li (or Na)-ion battery with fast electrode kinetics and super-long life*. Science Advances, 2016. 2(1): p. e1501038.
62. Aricò, A.S., et al., *Nanostructured materials for advanced energy conversion and storage devices*. Nature Materials, 2005. 4: p. 366.
63. Wang, J., et al., *Pseudocapacitive Contributions to Electrochemical Energy Storage in TiO2 (Anatase) Nanoparticles*. The Journal of Physical Chemistry C, 2007. 111(40): p. 14925-14931.
64. Weppner, W. and R.A. Huggins, *Determination of the Kinetic Parameters of Mixed-Conducting Electrodes and Application to the System Li3Sb*. Journal of The Electrochemical Society, 1977. 124(10): p. 1569-1578.
65. Rui, X.H., et al., *Analysis of the chemical diffusion coefficient of lithium ions in Li3V2(PO4)3 cathode material*. Electrochimica Acta, 2010. 55(7): p. 2384-2390.
66. Zhang, N., et al., *Cation-Deficient Spinel ZnMn2O4 Cathode in Zn(CF3SO3)2 Electrolyte for Rechargeable Aqueous Zn-Ion Battery*. Journal of the American Chemical Society, 2016. 138(39): p. 12894-12901.
67. Tong, Z., et al., *Improved electrochromic performance and lithium diffusion coefficient in three-dimensionally ordered macroporous V2O5 films*. Journal of Materials Chemistry C, 2014. 2(18): p. 3651-3658.
68. Mohamedi, M., et al., *Electrochemical investigation of LiNi0.5Mn1.5O4 thin film intercalation electrodes*. Electrochimica Acta, 2002. 48(1): p. 79-84.
69. Xie, J., et al., *Li-ion diffusion kinetics in LiFePO4 thin film prepared by radio frequency magnetron sputtering*. Electrochimica Acta, 2009. 54(20): p. 4631-4637.
70. Liu, H., et al., *Kinetic study on LiFePO4/C nanocomposites synthesized by solid state technique*. Journal of Power Sources, 2006. 159(1): p. 717-720.
71. Lu, Y., et al., *Facile Synthesis of Na0.33V2O5 Nanosheet-Graphene Hybrids as Ultrahigh Performance Cathode Materials for Lithium Ion Batteries*. ACS Applied Materials & Interfaces, 2015. 7(31): p. 17433-17440.